Foliage Clumping Index Over China's Landmass Retrieved From the MODIS BRDF Parameters Product

Gaolong Zhu, Weimin Ju, Jing M. Chen, Peng Gong, Bailing Xing, and Jingfang Zhu

***Abstract*—The three-dimentional plant canopy architecture is often characterized using the foliage clumping index useful for ecological and land surface modeling. In this paper, an algorithm is developed to retrieve the foliage clumping index with the Moderate Resolution Imaging Spectroradiometer bidirectional reflectance distribution function (BRDF) parameter product (MCD43A1), which is generated using the RossThick-LiSparse Reciprocal (Ross–Li) model. First, the Ross–Li model is modified to improve the simulation of the reflectance at hotspot using the Polarization and Directionality of Earth Reflectance measurements as benchmarks to determine BRDF parameters. Then, the modified model (Ross–Li-H) is used to simulate the reflectance at hotspot and darkspot, which is used to calculate the normalized difference between hotspot and darkspot (NDHD). With the relationship between clumping index and NDHD simulated by the 4-Scale geometrical model, the clumping index over China's landmass at 500-m resolution is retrieved every 8 days during the period from 2003 to 2008. Finally, The effect of topography on the retrieved clumping index is corrected using a topographic compensation function calculated from the digital elevation model at 90-m resolution. The topographically corrected clumping index values correlate well with field measurements at five sites over China, indicating the feasibility of the algorithm for retrieving the clumping index from the MCD43A1 product.**

***Index Terms*—Clumping index, hotspot, Moderate Resolution Imaging Spectroradiometer (MODIS), normalized difference between hotspot and darkspot (NDHD), Polarization and Directionality of Earth Reflectance (POLDER).**

Manuscript received January 13, 2011; revised May 17, 2011; accepted September 11, 2011. Date of publication November 21, 2011; date of current version May 16, 2012. This work was supported in part by the National Basic Research Program of China (973 Program) under Contact 2010CB833503 and 2010CB950702, by the National 863 Program of China under Contact 2009AA12Z134, by the Priority Academic Program Development (PAPD) of Jiangsu Higher Education Institutions, and by the Fundamental Research Funds for the Central Universities.

G. Zhu was with the International Institute for Earth System Sciences, Nanjing University, Nanjing 210093, China. He is now with the Department of Geography, Minjiang University, Fuzhou 350108, China (e-mail: zhugaolong@163.com).

W. Ju, B. Xing, and J. Zhu are with the International Institute for Earth System Sciences, ICGCR, Nanjing University, Nanjing 210093, China (email: juweimin@nju.edu.cn; xingjinxuan@163.com; zdzhujingfang@163.com).

J. M. Chen is with the International Institute for Earth System Sciences, Nanjing University, Nanjing 210093, China and also with the Department of Geography, University of Toronto, Toronto, ON M5S 3G3, Canada (e-mail: chenj@geog.utoronto.ca).

P. Gong is with the Ministry of Education Key Laboratory for Earth System Modelling, Center for Earth System Science, Tsinghua University, Beijing 100084, China and also with the Department of Environmental Science, Policy and Management, University of California, Berkeley, CA 94720 USA (e-mail: gong@irsa.ac.cn).

Color versions of one or more of the figures in this paper are available online at http://ieeexplore.ieee.org.

Digital Object Identifier 10.1109/TGRS.2011.2172213

I. Introduction

THE FOLIAGE clumping index (Ω)[1] quantifies the spatial distribution of leaves within distinct vegetation structures such as tree groups, tree crowns, whorls, branches, and shoots [2]. It is an important parameter for ecological, hydrological, and land surface models [3], [4] and for retrieving other vegetation structural parameters from remote sensing data, such as leaf area index (LAI). This parameter is an indispensable correction factor to convert the effective LAI (Le) [5], which assumes a random distribution of leaves in space, to the true LAI [6]–[8]. It is also needed for the separation of the canopy into sunlit and shaded leaves, which is crucial for accurate simulations of photosynthesis and evapotranspiration [9]–[11].

Natural vegetation canopies are often clumped. Foliage clumping varies considerably with land cover type, vegetation development stage, and season, making it difficult to retrieve this parameter reliably at regional scales. It is even difficult to measure it accurately in the field because foliage clumping often occurs at many levels: shoot [2], between-crown [12], and ecosystem [13]. Tracing radiation and architecture of canopies (TRAC) [14], digital hemispheric photography, and multiband vegetation imagers have been practically used to measure the clumping index in various ecosystems over the world [6], [15]–[17]. However, measurements by these three instruments are significantly different in some sites [18].

Currently, clumping index values are often assumed to vary only with land cover types in most operational LAI retrieval algorithms and ecological models [19], [20]. Such simplification can induce large uncertainties in the retrieved LAI and modeled ecological results. For example, the net and gross ecosystem primary productivity may be considerably underestimated when foliage clumping is ignored in the Boreal Ecosystem Productivity Simulator (BEPS) model [4]. Lacaze *et al.* [21] reported that the estimation of daily canopy photosynthesis can differ by 20% for a black spruce stand if the clumping effect is ignored. Therefore, it is highly desirable to map the clumping index from remote sensing data for different types of biomes for improving the retrieval of LAI and model simulations.

The bidirectional reflectance distribution function (BRDF) measured by multi-angular remote sensing is an intrinsic property characterizing the anisotropy of surface reflectance, which contains the structural information of vegetated surfaces [4], [7], [22]–[27]. Several angular indices calculated from the combination of some specific directional reflectance or linear kernel-driven BRDF model parameters have been proposed to

retrieve the clumping index using multi-angular remote sensing data. Roujean and Lacaze [7] retrieved the clumping index from the vertical difference vegetation index (DVI_0), which was calculated as the difference between the values of isotropic kernel for near infrared (NIR) and visible bands. Chen *et al.* [28] and Lacaze *et al.* [21] proposed that clumping index is linearly correlated with the hotspot and darkspot index (HDS). Chen *et al.* [4] suggested that the improved angular index named normalized difference between hotspot and darkspot (NDHD) may be more linearly related to the clumping index than HDS. The applicability of NDHD in retrieving the clumping index has been recently proved by ground measurements [17], [29]. These studies have demonstrated the potential to retrieve the clumping index from hotspot and darkspot reflectance.

The global and continental clumping index maps have been generated using 6-km multi-angular Polarization and Directionality of Earth Reflectance (POLDER) data [4], [7], [21], [29]–[31]. The reliability and accuracy of these maps have been validated using various independent field measurements taken in different regions and seasons [7], [17], [32]. The availability of such clumping index products would definitely improve the performance of regional/global ecological, hydrological, and land surface models. However, the spatial resolution of currently available clumping index maps is relatively low (6 km) and cannot fully satisfy the requirements of regional/global ecological, hydrological, and climate models. Therefore, efforts should be made to improve the spatial resolution of clumping index maps using presently available remote sensing data.

The main objectives of this study are: 1) to explore the feasibility of deriving the clumping index at 500-m resolution based on NDHD, which is calculated from the Moderate Resolution Imaging Spectroradiometer (MODIS) BRDF parameters product in the NIR band; 2) to validate the retrieved clumping index with ground measurements; and 3) to analyze the spatial and temporal variations of the retrieved clumping index in China.

II. Data Used and Methods

A. Remote Sensing Data

The POLDER-3 instrument onboard the PARASOL microsatellite is a radiometer designed to measure the directional and polarized reflectance of the surface-atmosphere system. It provides an adequate directional sampling of every point on the Earth with view angles up to 60°–70° and a full azimuth range, at a spatial resolution of about 6 km, when the atmospheric conditions are favorable [33]. The monthly global POLDER-3/PARASOL BRDF data set built by the Laboratoire des Sciences du Climat et de l'Environnement (LSCE) is used in this study. This data set contains the highest quality BRDFs of POLDER-3 at 490, 565, 670, 765, 865, and 1020 nm for each month during the period from November, 2005 to October, 2006. Totally, there are 20985 thematically homogeneous pixels based on the GLC2000 classification system in this data set. The percentage of thematic homogeneity within each pixel is higher than 80%. The data of BRDFs for each pixel consist of the surface reflectance in each band at different view angles acquired in a certain month, latitude and longitude, GLC2000 land cover type, normalized difference vegetation index (NDVI), percentage of homogeneity, date of observation, solar zenith angle, view zenith angle, and relative azimuth angle. On average, there are 132 valid observations from different angles for a POLDER-3 pixel in a month (Fig. 1). With the assumption that surface properties change little during this period of time, POLDER-3 can provide an adequate sampling of directional space for a given pixel to reconstruct BRDF of surface targets, including the exact observations at the hotspot [34].

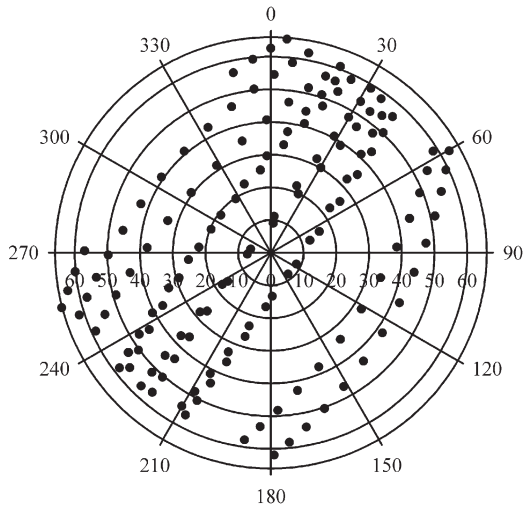

Fig. 1. Example of the BRDF sampling of a POLDER-3 pixel (24.64N, 105.52W) in February 2006. The radius represents view zenith angle (°), and the polar angle represents relative azimuth angle (°). The solar zenith angle of these observations by POLDER-3 ranges from 36.4° to 40.1°.

The MODIS BRDF model parameters product (MCD43A1) provides the weighting parameters associated with the RossThick-LiSparse Reciprocal BRDF model (Ross–Li model) that describes the anisotropy of surface reflectance. This product is operationally generated using following linear kernel-based semi-empirical model [35]–[38]:

$$R(\theta,\vartheta,\phi,\Lambda) = f_{\rm iso}(\Lambda) + f_{\rm geo}(\Lambda)K_{\rm geo}(\theta,\vartheta,\phi) + f_{\rm vol}(\Lambda)K_{\rm vol}(\theta,\vartheta,\phi) \quad (1)$$

$$K_{\rm vol}(\theta,\vartheta,\phi) = \frac{(\pi/2-\xi)\cos\xi+\sin\xi}{\cos\theta+\cos\vartheta} - \frac{\pi}{4} \quad (2)$$

$$K_{\rm geo}(\theta,\vartheta,\phi) = O(\theta,\vartheta,\phi) - \sec\theta - \sec\vartheta + \frac{1}{2}(1+\cos\xi)\sec\theta\sec\vartheta \quad (3)$$

$$O(\theta,\vartheta,\phi) = \frac{1}{\pi}(t-\sin t\cos t)(\sec\theta+\sec\vartheta) \quad (4)$$

$$\cos t = 2\frac{\sqrt{D^2+(\tan\theta\tan\vartheta\sin\phi)^2}}{\sec\theta+\sec\vartheta} \quad (5)$$

$$D = \sqrt{\tan^2\theta+\tan^2\vartheta-2\tan\theta\tan\vartheta\cos\phi} \quad (6)$$

$$\cos\xi = \cos\theta\cos\vartheta+\sin\theta\sin\vartheta\cos\phi \quad (7)$$

where $R(\theta, \vartheta, \phi, \Lambda)$ is the directional reflectance in waveband Λ; K_{geo} and K_{vol} are the geometric optical kernel (LiSparse Reciprocal kernel) and volumetric scattering kernel (RossThick kernel), respectively, and are functions of solar zenith angle (θ), view zenith angle (ϑ), and relative azimuth angle (ϕ); $f_{\text{iso}}(\Lambda)$, $f_{\text{geo}}(\Lambda)$, and $f_{\text{vol}}(\Lambda)$ are the weights for the isotropic, geometric, and volumetric kernels in waveband Λ, respectively; and ξ is the scattering angle, i.e., the angle between the sensor and the sun relative to the target. With these three BRDF parameters, the Ross–Li model is able to simulate the directional reflectance at any desired illumination and view angles.

The MCD43A1 product is generated every 8 days from the multi-angular reflectance observations of MODIS onboard Terra and Aqua acquired in 16 days. MCD43A1 is provided as a level-3 gridded product in the Sinusoidal projection at 463.3-m spatial resolution. The quality assessment (QA) information of MCD43A1 is correspondingly provided in MCD43A2, with $QA = 0$ for best quality, full inversion, $QA = 1$ for good quality, full inversion, $QA = 2$ for magnitude inversion (number of observations > 7), $QA = 3$ for magnitude inversion (number of observations $>= 3$ & < 7), and $QA = 4$ for filled values.

B. Validation of the Ross–Li Model Using POLDER-3 Data

The accuracy assessment of BRDF acquired from satellite sensors at coarse spatial resolution is not straightforward [39]. One possible strategy to validate a BRDF product is to compare BRDF measurements from different spaceborne or airborne sensors on a homogeneity landscape [39]. The NIR channel of MODIS covers a spectral domain from 841 to 876 nm. The NIR band of POLDER-3 is centered near 865 nm with a bandwidth of 40 nm. Both the POLDER-3 BRDF data and the MODIS BRDF model parameters product (MCD43A1) are derived from the geocoded, calibrated, atmospherically corrected, and cloud-screened input data measured over multidate periods. Since the land cover types of selected POLDER-3 pixels are almost homogenous (The coverage of a dominant cover in a POLDER-3 pixel is above 80%), the scale difference between POLDER-3 and MODIS data is expected to be small and hence ignored in this study. Therefore, it is practical to use the surface directional reflectance observed by the POLDER-3 instrument as a benchmark for evaluating the accuracy of NIR reflectance simulated by the Ross–Li BRDF model despite the slight difference in the NIR spectral domain of these two sensors.

In this paper, 1193 tiles of MCD43A1 and MCD43A2 data acquired between November 2005 and October 2006 are downloaded from the Land Processes Distributed Active Archive Center (LP DAAC). The POLDER-3 and MCD43A1 data are both in the Sinusoidal projection. The size of a POLDER-3 pixel approximately equals that of 13×13 MODIS pixels. If the data of 169 MODIS pixels are all in the best or good quality (MODIS $QA = 0$ or 1), the average simulated directional reflectance of 169 pixels is compared with the POLDER-3 data acquired in the same period. For each MODIS pixel, the directional reflectance is simulated with the Ross–Li model driven by the MCD43A1 BRDF parameters and corresponding solar zenith, view zenith, and relative azimuth angles extracted from the POLDER-3 BRDF data set. Among all 20,985 pixels in the POLDER-3 BRDF data set, only 9961 vegetation pixels with 714,652 observations under different angular conditions are selected with the criteria that the NDVI value of a POLDER-3 pixel is above 0.15 and corresponding MCD43A1 products of 169 MODIS pixels are in the best or good quality (MODIS $QA = 0$ or 1). These 9961 pixels are distributed globally and belong to different land cover types (Fig. 2).

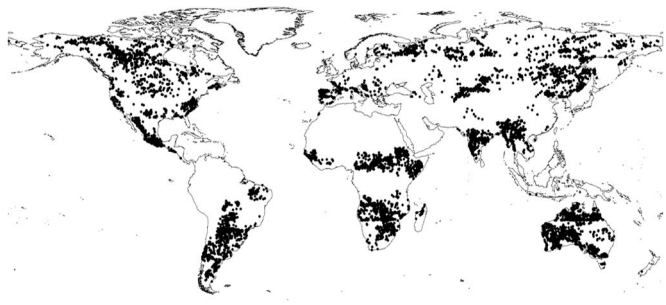

Fig. 2. Distribution of 9961 pixels extracted from POLDER-3 BRDF data set used to validate MODIS BRDF model parameter product.

C. Modifications for the Ross–Li Model

The hotspot reflectance, which occurs when the illumination and view directions coincide, is needed for the reliable retrieval of clumping index. Although MODIS does not directly capture the hotspot signal due to its design and orbit limitations, the hotspot reflectance can be obtained through extrapolating using the kernel-based Ross–Li model. This model has been found to underestimate the hotspot magnitude because the correlation between the solar beam and the view line within the same canopy gap is not considered in kernel-based models [41], [42]. The comparison between the POLDER-3 data and reflectance simulated using the original Ross–Li model driven by the MCD43A1 data confirms this hotspot underestimation problem (see Section III). Several studies have been previously conducted to improve the BRDF model for simulating the hotspot signals. Chen and Cihlar [41] proposed a hotspot function based on the canopy gap size distribution theory [40] to correct the underestimation of hotspot reflectance simulated by the kernel-based model. The directional reflectance is simulated as

$$Rc(\theta, \vartheta, \phi, \Lambda) = (f_{\text{iso}}(\Lambda) + f_{\text{geo}}(\Lambda) K_{\text{geo}}(\theta, \vartheta, \phi) + f_{\text{vol}}(\Lambda) K_{\text{vol}}(\theta, \vartheta, \phi)) \left(1 + C_1 \mathrm{e}^{(-\xi/\pi) C_2}\right) \quad (8)$$

where ξ is the scattering angle. C_1 and C_2 are two parameters controlling the magnitude and width of the hotspot, respectively, and vary with land cover types. Equation (8) is named as the Ross–Li-C model hereinafter. This model can simulate well the peak reflectance at hotspot observed by the Advanced Very High Resolution Radiometers (AVHRR) [41].

Maignan *et al.* [42] proposed an algorithm to improve the simulation of hotspot reflectance through only modifying the

RossThick kernel, i.e.,

$$K_{\mathrm{vol\_M}}(\theta,\vartheta,\phi)=\frac{(\pi/2-\xi)\cos\xi+\sin\xi}{\cos\theta+\cos\vartheta}\times\left(1+(1+\xi/\xi_0)^{-1}\right)-\frac{\pi}{4} \quad (9)$$

where ξ_0 is a characteristic angle that can be related to the ratio of the scattering element size to the canopy vertical density, and it takes a constant value of 1.5° [42]. This model is named as the Ross–Li-M model hereinafter.

Compared with the Ross–Li-C model, the Ross–Li-M model is simpler and has no parameters to be assigned (such as C_1 and C_2 in the Ross–Li-C model). However, validations show that the Ross–Li-M model overestimates hotspot reflectance due to the overcorrection of the RossThick kernel when ξ approaches zero (see Section III). To improve the simulation of hotspot reflectance, a new model which combines the Ross–Li-C model and Ross–Li-M model is developed as follows:

$$R_{\mathrm{H}}(\theta,\vartheta,\phi,\Lambda)=f_{\mathrm{iso}}(\Lambda)+(1+A\mathrm{e}^{-\xi/\xi_0})f_{\mathrm{geo}}(\Lambda)K_{\mathrm{geo}}(\theta,\vartheta,\phi)+(1+B\mathrm{e}^{-\xi/\xi_0})f_{\mathrm{vol}}(\Lambda)K_{\mathrm{vol}}(\theta,\vartheta,\phi) \quad (10)$$

where A and B are two parameters used to adjust the hotspot magnitude caused by geometrical and volumetric scattering. ξ_0 is a parameter to control the hotspot width. This model is named as Ross–Li-H model hereinafter.

D. Determining Parameters for the Ross–Li-C and Ross–Li-H Models

To optimize the C_1 and C_2 values in the Ross–Li-C model, 3572 pixels of different land cover types with at least one observation near the hotspot ($\xi<5^\circ$) for each pixel are extracted from the above POLDER-3 BRDF data set. The NIR reflectance of 169 MODIS pixels within a POLDER pixel is individually simulated using the Ross–Li-C model based on the corresponding MCD43A1 data and different combinations of C_1 and C_2 values. The NIR reflectance of 169 MODIS pixels is averaged and compared with POLDER-3 observed data. C_1 is allowed to increase from 0 to 1 at steps of 0.01, and C_2 is allowed to increase from 0 to 120 at steps of 0.5. The optimum C_1 and C_2 values for each pixel are determined when the root mean square error (RMSE) of simulated NIR reflectance by the Ross–Li-C model reaches the minimum value. The optimum C_1 and C_2 values for a specific land cover type are the averages of optimized C_1 and C_2 of different pixels belong to this land cove type.

The optimal values of A, B, and ξ_0 in the Ross–Li-H model are determined using a multivariate regression method. First, the NIR reflectance observed by POLDER-3 (R_{P}) is supposed to equal the reflectance simulated by the Ross–Li-H model, i.e.,

$$R_{\mathrm{P}}=f_{\mathrm{iso}}(\Lambda)+(1+A\mathrm{e}^{-\xi/\xi_0})f_{\mathrm{geo}}(\Lambda)K_{\mathrm{geo}}(\theta,\vartheta,\phi)+(1+B\mathrm{e}^{-\xi/\xi_0})f_{\mathrm{vol}}(\Lambda)K_{\mathrm{vol}}(\theta,\vartheta,\phi). \quad (11)$$

Then, the above equation can be rewritten as

$$\left(R_{\mathrm{P}}-R(\theta,\vartheta,\phi,\Lambda)\right)/\mathrm{e}^{-\xi/\xi_0}=Af_{\mathrm{geo}}(\Lambda)K_{\mathrm{geo}}(\theta,\vartheta,\phi)+Bf_{\mathrm{vol}}(\Lambda)K_{\mathrm{vol}}(\theta,\vartheta,\phi) \quad (12)$$

where $R(\theta,\vartheta,\phi,\Lambda)$ is the NIR reflectance simulated by the original Ross–Li model.

In the above (12), there are three unknown parameters (A, B, and ξ_0). If ξ_0 is given, this equation can be further simplified as a bivariate linear regression, and parameters A and B can be determined using the least squares fit method. The RMSE and R^2 of simulated reflectance can be correspondingly calculated. In this paper, ξ_0 is allowed to change from 0 to 10 at steps of 0.01 since the width of the hotspot is mostly smaller than 10°. If a combination of A, B, and ξ_0 values produce the minimum RMSE and maximum R^2, this set of A, B, and ξ_0 is used as the optimum parameters for the Ross–Li-H model.

Bréon *et al.* (2002) indicated that the hotspot width is related to cover type and is independent of wavelength. The hotspot half width ξ_0 of most targets is between 1° and 2°, with a range from 1° to 5°[43]. Therefore, a total of 6833 observations with the scattering angle (ξ) less than 5° are extracted from the above POLDER-3 BRDF data set as the observations of hotspot reflectance to determine A, B, and ξ_0. To limit the effect of nonuniform distribution of scattering angles of observations on the determinations of A, B, and ξ_0, these 6833 observations are grouped at 0.1° intervals of ξ. The mean POLDER-3 reflectance of each interval and the corresponding mean values of $R(\theta,\vartheta,\phi,\Lambda)$, $f_{\mathrm{geo}}(\Lambda)K_{\mathrm{geo}}$, and $f_{\mathrm{vol}}(\Lambda)K_{\mathrm{vol}}$ are used to determine parameters A, B, and ξ_0. The mean reflectance of large numbers of pixels of various cover types can moderate the effects of the variations of cover types, vegetation density, and solar zenith angle on the determination of parameters A, B, and ξ_0.

E. Retrieval of Clumping Index and Topographic Correction

The clumping index is retrieved from NDHD, which is defined as [4]

$$NDHD=(\rho_h-\rho_d)/(\rho_h+\rho_d) \quad (13)$$

where ρ_h and ρ_d are the reflectance at the hotspot and darkspot, respectively. The widely accepted explanation for the hotspot phenomenon is shadow hiding [43]. At the hotspot where the illumination and view directions coincide, all shadows are hidden by the surface targets that cast them, resulting in the maximum backscatter strength. The darkspot, on the other hand, contains the maximum shadows observed in the forward scattering direction, where the reflectance is minimum. Most of the clumping information is contained in the darkspot reflectance, which is determined by the vegetation density as well as the shape and size of foliage clumps (tree crowns, branches, shoots, shrubs, row crops, etc.) [30]. For a given solar zenith angle, the hotspot intensity mainly depends on the target optical properties and its structural characteristics. The ratio form of NDHD can minimize the influences of foliage optical properties and accentuates the structural information [30].

NDHD is found to be linearly related to the clumping index for the red and NIR bands when the canopy coverage is greater than 25% [30]. The relationship between NDHD and clumping index depends on the solar angle and the crown shape. Other forest structural parameters such as LAI, stand density, and canopy height have small effects on this relationship [30]. Pinty *et al.* [23] asserted that the red band provides better contrast between vertically clumped elements and the background due to weaker multiple scattering. However, a stronger relationship between NDHD and clumping index in the NIR band was found by Chen *et al.* [30] and Simic *et al.* [17] due to lower atmospheric noise in this band than in the red band for the spaceborne sensor. In this paper, only the MODIS BRDF model parameters with best or good quality (MODIS $QA = 0$ or 1) in the NIR band are used to retrieve the clumping index. The hotspot and darkspot reflectance in NIR band is simulated using (10) with the solar zenith angle and view zenith angle both set as 45°. The azimuth angle (ϕ) is set as 0° for hotspot reflectance simulation and 180° for darkspot reflectance simulation. These fixed angular configurations for hotspot and darkspot were proposed by several previous studies [25], [44], [45], and are used to calculated MODIS BRDF shape indicators [46]. Based on the findings of Chen *et al.* [30], a cone/cylinder crown shape is assumed for coniferous forests $(\Omega = -0.61NDHD + 0.82)$, and an ellipsoid for other vegetation types $(\Omega = -1.4NDHD + 1.28)$. The GLC2000 land cover map at 1-km resolution is resampled to 500-m resolution to determine the land cover type for each MODIS pixel.

Topography might have a severe impact on BRDF due to terrain shadowing, adjacent hill illumination, view factor effects, and/or the aspect and steepness of individual slopes [47]. The topographic shadows may enhance the reflectance contrast between hotspot and darkspot, which will lead to underestimation of the retrieved clumping index. Since most forests in China are located in mountainous areas, the terrain effects on clumping retrievals cannot be ignored. A topographic compensation approach proposed by Pisek *et al.* [29] is used in this study to correct the influence of topography on the retrieved clumping index. First, a digital elevation model (DEM) SRTM4.1 (Shuttle Radar Topography Mission) with 90-m resolution for the entire China is downloaded from International Centre for Tropical Agriculture website (http://srtm.csi.cgiar.org). The standard deviation (σ) of elevations is calculated within each MODIS pixel (463.3 m). All valid retrievals of the clumping index averaged over the growing seasons (from April to September) from 2003 to 2008 are binned into 25-m intervals of σ. The mean clumping index value (Ω_{m}) is calculated for every σ interval. Second, a cubic polynomial $(R^2 = 0.996)$ is fitted using the Ω_{m} values and corresponding medians of different σ intervals

$$\Omega_{\mathrm{T}} = -9.042 \times 10^{-10}\sigma^3 + 1.6 \times 10^{-6}\sigma^2 - 1.014 \times 10^{-3}\sigma + 0.755 \quad (14)$$

where Ω_{T} describes cross-biome, terrain shadow-induced decreasing trend in the topographically uncorrected Ω with increasing topographic variability, represented by σ [29]. In other words, the foliage clumping is assumed to be independent of σ in the derivation of Ω_{T} since the area fractions of different biome types vary in a limited range at each σ interval, which suppresses the foliage structural effects on the Ω_{T} derivation [29]. Therefore, for each MODIS pixel with topographic variability of σ_{i}, the terrain-induced clumping is equal to the difference δ between Ω_{T} at $\sigma = 0$ (flat terrain) and Ω_{T} at $\sigma = \sigma_{\mathrm{i}}$. Finally, the effect of topography is removed by added δ to the topographically uncorrected Ω for each pixel in the clumping index map.

F. Clumping Index Field Measurements

To validate the retrieved clumping index, field measurements of this parameter were conducted at five sites in China from April to September, 2009 (see Table III). The vegetation types include broadleaf, needle-leaf, and mixed forests, shrubs, and bamboos. About 75 plots in these sites were located on relatively flat terrains and covered by relatively homogeneous vegetation types. Two 50-m parallel transects perpendicular to the sunray and separated by 25 m were laid in the center of each plot. These transects were marked every 10 m. The TRAC instrument was used to measure sunfleck widths along these transects beneath the canopies in cloud-free conditions at a steady pace (about 0.3 m/s). The location of each plot was measured using a GPS device.

TRAC can only measure the element clumping index (Ω_{E}), which quantifies clumping effects at scales larger than the shoot. TRACWin was used to compute Ω_{E}. The Ω_{E} of a plot is the mean of ten segment measurements at the plot. The total clumping index Ω is calculated as

$$\Omega = \Omega_{\mathrm{E}}/\gamma_{\mathrm{E}} \quad (15)$$

where γ_{E} is the ratio of needles to shoots for needle-leaf species, which accounts for the clumping of needles into shoots [48]. For broadleaf forests, γ_{E} is set as 1.0. For other species, γ_{E} values are determined by empirical values [49], [50].

The plot-level measured clumping index is used for validating the clumping index retrieved using the MODIS BRDF products. The direct use of clumping index measurements at the plot level to validate the results retrieved from MCD43A1 data is an approximation due to the difference in the sizes of the plots and MODIS pixels (463.3 m). The local field-level measurements should be optimally integrated with high-resolution imagery to validate the moderate-resolution remote sensing products [51]. Unfortunately, no high-resolution maps of the clumping index are currently available, except for one made by Simic *et al.* [17] with a limited spatial coverage, to allow a real product validation. There are currently no high-resolution multi-angular remote sensing data available in China for us to retrieve high-resolution clumping index maps to validate this parameter retrieved from MCD43A1 data in this study. Pisek *et al.* [29] pointed out that the clumping index measured by TRAC is the most suitable for comparison with the moderate resolution clumping index product since the instrument allows to sample in extensive spatial coverage. The relatively flat terrains and homogeneous vegetation types of plots selected in this study

TABLE I
VALUES OF C_1 AND C_2 IN THE ROSS–LI-C MODEL FOR DIFFERENT COVER TYPES DERIVED FROM POLDER-3 DIRECTIONAL REFLECTANCE AND MODIS BRDF MODEL PARAMETERS PRODUCT. THE STANDARD DEVIATIONS OF C_1 AND C_2 WITHIN EACH COVER TYPE ARE ALSO SHOWN

GLC2000 Cover Type	C_1	C_2	$STDV_{C1}$	$STDV_{C2}$
Tree Cover, broadleaved, evergreen	0.302	26.6	0.088	13.6
Tree Cover, broadleaved, deciduous, closed	0.296	33.8	0.077	16.9
Tree Cover, broadleaved, deciduous, open	0.296	26.4	0.112	15.3
Tree Cover, needle-leaved, evergreen	0.333	31.8	0.109	17.7
Tree Cover, needle-leaved, deciduous	0.370	32.5	0.099	17.9
Tree Cover, mixed leaf type	0.268	23.6	0.091	12.6
Tree Cover, regularly flooded, fresh water	0.200	8.5	0.085	4.2
Tree Cover, regularly flooded, saline water	0.240	35.8	0.076	21.3
Mosaic: Tree Cover/Other natural vegetation	0.334	24.3	0.099	11.8
Tree Cover, burnt	0.333	21.7	0.099	10.1
Shrub Cover, closed-open, evergreen	0.308	31.9	0.110	16.7
Shrub Cover, closed-open, deciduous	0.241	27.2	0.079	16.6
Herbaceous Cover, closed-open	0.246	27.8	0.091	16.6
Sparse herbaceous or sparse shrub cover	0.215	28.0	0.067	14.6
Regularly flooded shrub and/or herbaceous cover	0.232	30.5	0.066	16.5
Cultivated and managed areas	0.245	27.1	0.081	14.5
Mosaic: Cropland/Tree Cover/Other natural vegetation	0.236	18.7	0.064	9.2
Mosaic: Cropland / Shrub and/or grass cover	0.278	32.3	0.092	15.8
Bare Areas	0.155	38.1	0.054	13.0

can partially constrain the scale effect on the difference between measured and retrieved clumping index.

III. RESULTS AND DISCUSSION

A. Optimized Parameters for the Ross–Li-C and Ross–Li-H Models

Table I shows the averages of optimized C_1 and C_2 of the NIR band for different land cover types in the Ross–Li-C model. The hotspot magnitude coefficient C_1 value for forest is larger than those for cropland and grassland. Needle-leaf deciduous forest has the largest C_1 value equal to 0.37, while barren land has the smallest C_1 value equal to 0.155. Forest has more distinct and heterogeneous canopy structure than grassland, cropland, and barren land, resulting in a relatively large hotspot magnitude. C_1 optimized here is much smaller than the values reported by Chen and Cihlar [41] for the AVHRR data. They used 0.40, 0.65, 0.60, and 0.50 for cropland, forest, barren, and grassland, respectively. The hotspot width parameter C_2 varies from 8.5 to 35.8. The mean C_2 value of 29.1 for forest corresponds to the mean hotspot half width ξ_0 of 6.2°($\xi_0 = 180/C_2$), which is somewhat larger than the value introduced by Bréon *et al.* [43]. In contrast, C_2 optimized here is considerably larger than the values of 8.33, 12.5, 12.5, and 8.33 used by Chen and Cihlar [41] for cropland, forest, barren, and grassland, respectively. We believe that the new C_1 and C_2 values found in this study are more reliable than those found in Chen and Cihlar [41] as POLDER-3 instrument can measure at angles much closer to the hotspot than AVHRR. However, the intraclass variability of the values of C_1 or C_2 is significant, as indicated by their relatively large standard deviations for each land cover type (Table I).

Fig. 3 shows the changes in R^2 and RMSE of the hotspot reflectance of NIR simulated by the Ross–Li-H model using the optimized parameters A and B with the hotspot half width ξ_0. When ξ_0 is less than 2°, R^2 is below 0.035. When ξ_0 is larger than 2°, R^2 increases quickly with ξ_0 and approaches the peak value of 0.62 at ξ_0 equal to 4.18°. If ξ_0 further increases, R^2 starts to decrease. The RMSE of simulated reflectance shows different changes with ξ_0 from R^2. With ξ_0 increasing from 1° to 4°, RMSE decreases quickly from 1.147 to 0.009. When ξ_0 is larger than 4°, RMSE increases slightly with increasing ξ_0. The optimized parameters A and B in the Ross–Li-H model are correlated with the hotspot half width ξ_0. When ξ_0 is smaller than 3°, parameter A increases quickly, and parameter B decreases quickly with the increase in ξ_0. Both parameters A and B slowly approach their asymptotes at ξ_0 above 3°. When ξ_0 equals 4°, the RMSE of simulated reflectance minimizes at a value of 0.009 and corresponding R^2 value equals 0.6, only slightly smaller than the maximum value of 0.62. Corresponding to ξ_0 equal to 4°, the optimized A and B are 0.52, and 1.60, respectively. These values are used in the Ross–Li-H model.

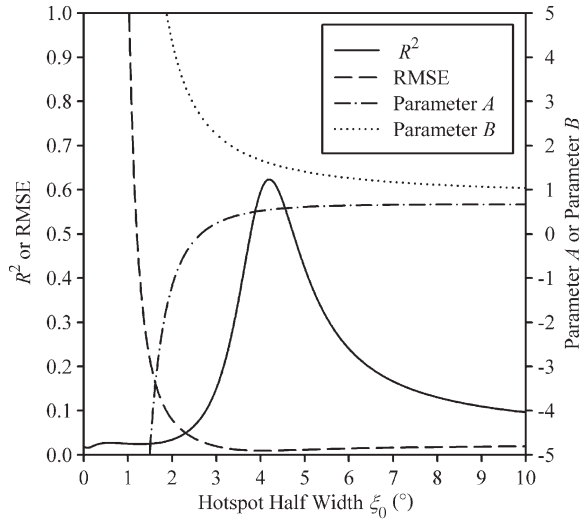

Fig. 3. Optimal parameters A and B of the NIR band in Ross–Li-H model change with the hotspot half width ξ_0 assigned in the Ross–Li-H model. The optimal parameters A and B corresponding to a given ξ_0 are determined by the least squares fit between the hotspot reflectance in the NIR band observed by POLDER-3 instrument and that simulated by the Ross–Li-H model. The R^2 and RMSE of each pair of A and B are also showed.

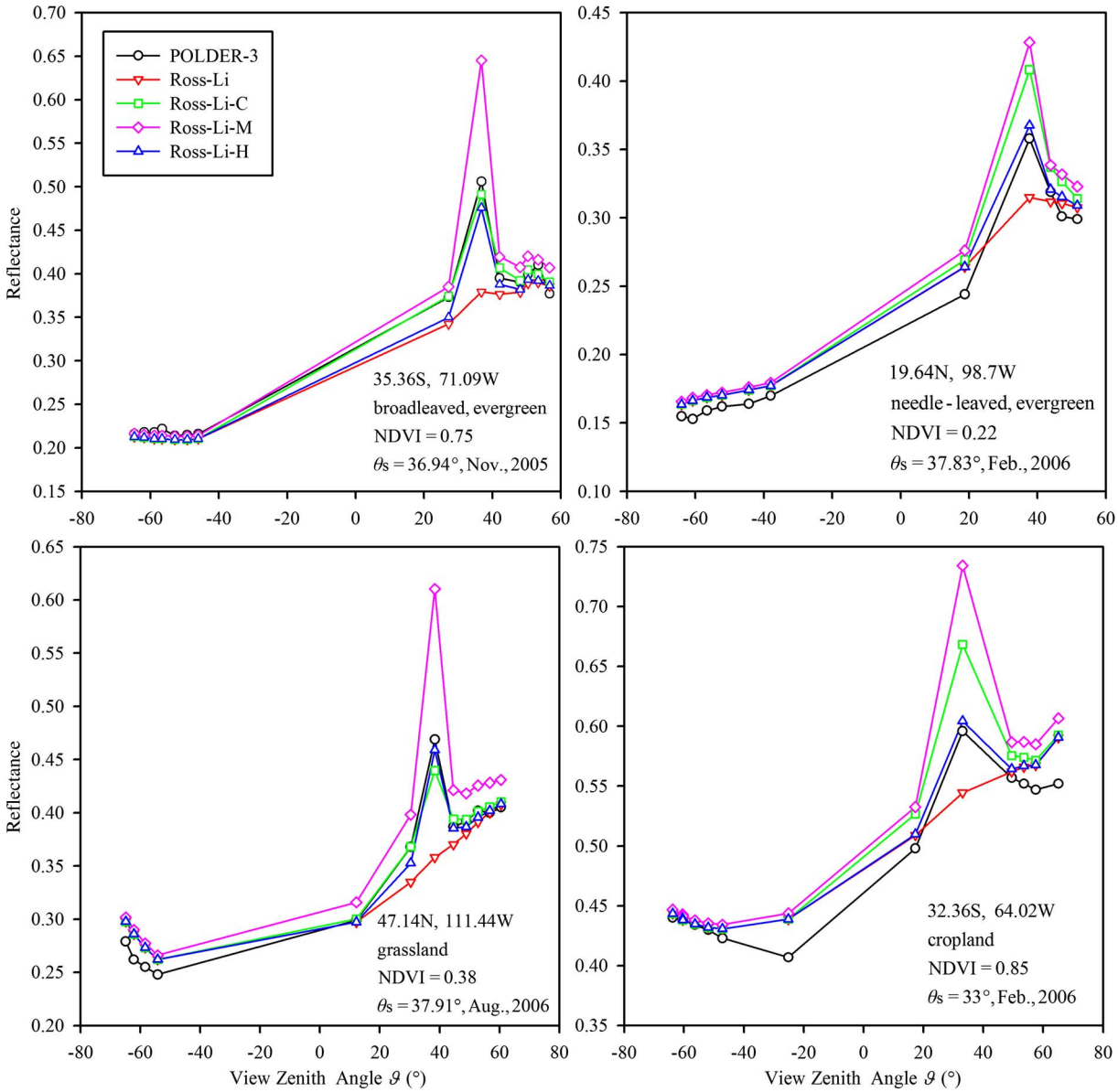

Fig. 4. Comparison of the directional reflectance at 865 nm simulated by the Ross–Li model, Ross–Li-C, Ross–Li-M, and Ross–Li-H based on MCD43A1 BRDF model parameters along the principal plane with POLDER-3 observations for four representative land cover types. The positive values in x-axis denote backward reflectance, and negative values indicate forward reflectance.

B. Comparison of Simulated Directional Reflectance With POLDER-3 Data

Fig. 4 shows the comparison of the directional reflectance along the principal plane simulated by the aforementioned BRDF models (Ross–Li, Ross–Li-C, Ross–Li-M, and Ross–Li-H) driven by the MCD43A1 BRDF parameters with the POLDER-3 observations for four typical pixels of different land cover types. The Ross–Li model is able to reproduce reflectance close to POLDER-3 data in most cases. However, it significantly underestimates the hotspot reflectance. In contrast, three modified BRDF models are all able to capture the reflectance peaks at and near the hotspot. However, compared with the observations of POLDER-3, the Ross–Li-M model overestimates hotspot reflectance due to its overcorrection for the RossThick kernel when ξ approaches zero. The Ross–Li-H model successfully simulates the observed BRDFs along the principal plane of these pixels, including the reflectance of hotspot and darkspot.

A total of 6833 observations of NIR reflectance near the hotspot ($\xi \leq 5^\circ$) are selected from the POLDER-3 data set to test the ability of aforementioned BRDF models (Ross–Li, Ross–Li-C, Ross–Li-M, and Ross–Li-H) to simulate reflectance close to the hotspot (Fig. 5). Overall, the hotspot reflectance simulated by the Ross–Li model is 14% lower than the POLDER-3 observations. The underestimation is larger for higher reflectance observed by POLDER-3. The R^2 and RMSE of reflectance near the hotspot simulated by the Ross–Li model are 0.847 and 0.069, respectively. The failure of the Ross–Li model to simulate the hotspot signal is mainly caused by the inability of its volumetric scattering kernel to account for the hotspot effect [36], [42]. Although the geometric optical kernel of the Ross–Li model has a peak value at the hotspot [35],

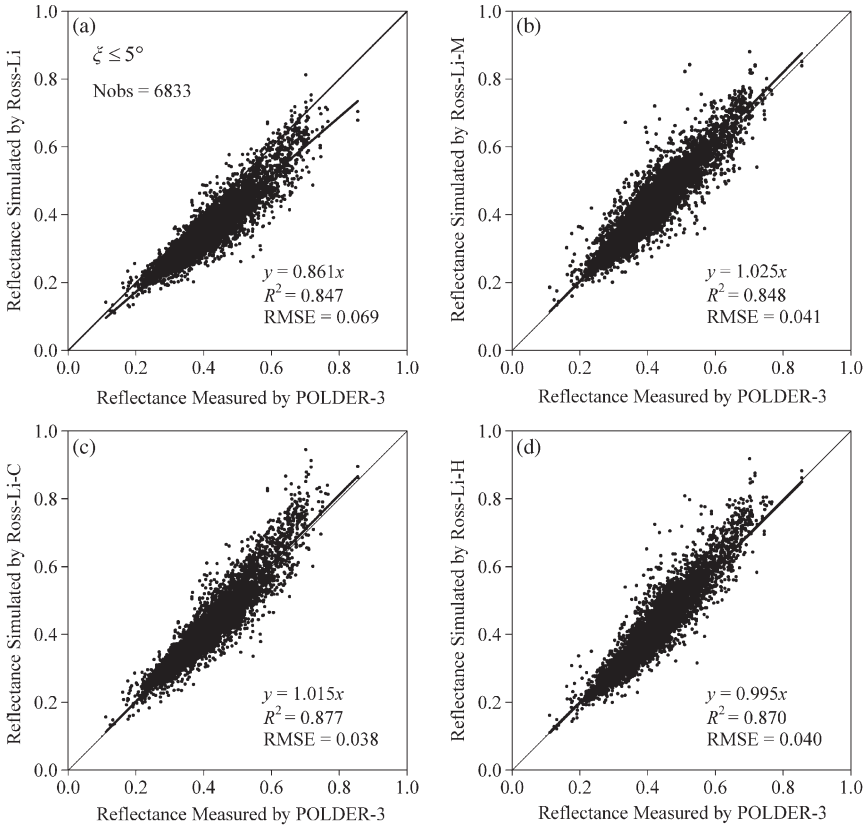

Fig. 5. Comparison of the 865-nm reflectance near the hotspot (scattering angle smaller than 5°) simulated by (a) the Ross–Li model, (b) Ross–Li-M model, (c) Ross–Li-C model, and (d) the Ross–Li-H model with POLDER-3 observations.

this peak is not large enough to capture the hotspot signal. The geometric optical kernel also needs further correction.

Three modified Ross–Li models substantially improve the simulation of reflectance near the hotspot. The Ross–Li-C model overperforms other models in reproducing directional reflectance near the hotspot, with the highest R^2 value of 0.877 and the smallest RMSE value of 0.038. The Ross–Li-H model demonstrates the ability similar to the Ross–Li-C model to simulate the hotspot reflectance, with R^2 and RMSE equal to 0.87 and 0.040, respectively. The Ross–Li-M model performs relatively poorer than the Ross–Li-C and Ross–Li-H models, but still much better than the original Ross–Li model in simulating reflectance near the hotspot.

The abilities of above models to simulate the hotspot ($\xi = 0^\circ$) and darkspot reflectance are further compared. The NIR directional reflectance of 714,652 observations by POLDER-3 and their simulations by the original and modified Ross–Li models are grouped at 1° intervals of ξ. The difference between the mean reflectance of each group observed by POLDER-3 and the corresponding simulations by each model are shown in Fig. 6. When ξ is smaller than 0.5° (close to the hotspot), the mean reflectance simulated by the original Ross–Li model is 0.1 smaller than the POLDER-3 data, which is in agreement with the conclusion drawn by Bréon *et al.* [43] that the hotspot reflectance amplitude is generally in the range of 0.1–0.2 at 865 nm. In contrast, the Ross–Li-M model overestimates hotspot reflectance by 0.075 in comparison with the POLDER-3 data. Both the Ross–Li-C and Ross–Li-H models improve the capabilities to reproduce the hotspot reflectance. The Ross–Li-H model performs slightly better than the Ross–Li-C model in simulating reflectance close to the hotspot ($\xi = 0^\circ$). When ξ is in the range from 20° to 110°, the

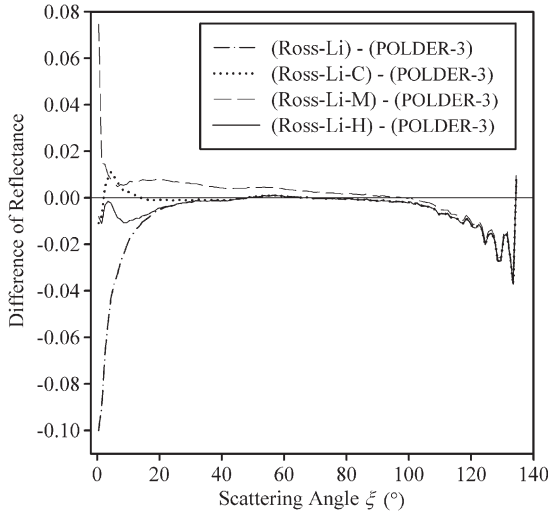

Fig. 6. Changes in the difference between the mean directional reflectance at 865 nm observed by POLDER-3 and simulated by models with scattering angle (ξ). The difference values are binned at one degree intervals of ξ. The dashed-dotted, dotted line, dashed, and solid lines represent results for the Ross–Li, Ross–Li-C, Ross–Li-M, and Ross–Li-H model models, respectively. Positive values mean that the simulated reflectance is larger than POLDER-3 data, vice versa. A total of 714 652 observations of POLDERT-3 are used in the comparison.

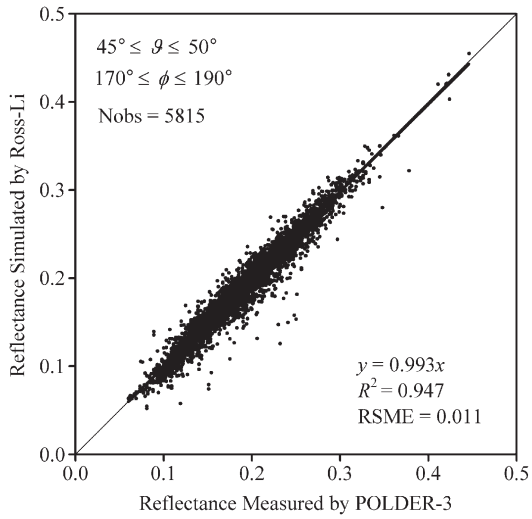

Fig. 7. Comparison of the darkspot reflectance at 865 nm simulated by the Ross–Li model and the POLDER-3 observations.

reflectance difference between the observations of POLDER-3 and the simulations by the original Ross–Li, Ross–Li-C, and Ross–Li-H models is very small, indicating the good ability of these models to simulate the observed BRDFs in most cases. Meanwhile, the reflectance simulated by the Ross–Li-M model is slightly larger than POLDER-3 observations. When ξ is larger than 110°, the original and modified Ross–Li models produce lower reflectance than POLDER-3 data. These errors may be related to the assumption of the LiSparse kernel in the Ross–Li model that the total area of vegetation and shadows should be much smaller than the total area of view field [52]. This assumption fails in the case of large view zenith angles or large solar zenith angles, resulting in large errors in simulating directional reflectance.

Reflectance observed by POLDER-3 with the view zenith angle ranging from 45° to 50° and the relative azimuth angle from 170° to 190° is selected to validate whether models are able to simulate reflectance near the darkspot. The darkspot reflectance simulated by the Ross–Li model is very close to the observations of POLDER-3 ($R^2 = 0.947$, $RMSE = 0.011$) (Fig. 7). As shown in Figs. 4 and 6, the darkspot reflectance simulated by three modified BRDF models is almost equivalent to that simulated by the Ross–Li model since ξ equals 90° for darkspot, making the correction factors [$e^{-\xi/\xi_0}$ in (8) and (10) or $(1+\xi/\xi_0)^{-1}$ in (9)] approach zero. The close agreement in darkspot between POLDER-3 and MODIS indicates that the NIR spectral difference is very small between these two sensors. The hotspot difference between the POLDER-3 observation and the MODIS BRDF product is mainly caused by the MODIS BRDF representation.

C. Spatial and Temporal Variations of the Retrieved Clumping Index in China

Since the Ross–Li-H model shows a better performance in simulating reflectance close to the hotspot, and it only has to determine two parameters (A and B) for all land cover types, it is used to simulate the hotspot and darkspot reflectance using 8-day MCD43A1 product for retrieving the clumping index. Clumping index maps of every 8 days are generated with simulated reflectance at hotspot and darkspot. Based on these 8-day maps, 36 maps of the monthly mean clumping index are calculated during the growing seasons (from April to September) for the years from 2003 to 2008. Topographical corrections are conducted for these maps using (14). Fig. 8 shows the spatial distribution of the average clumping index calculated from these 36 maps. The spatial distribution pattern of the clumping index is distinct and mirrors that of land cover types quite well (Fig. 9).

Grasslands have the largest clumping index, ranging from 0.8 to 1.0, due to their nearly random spatial distribution of foliage during the growing seasons. The clumping index of croplands is also high, ranging from 0.7 to 1.0. The nationwide means of clumping index for grasslands and croplands are in the range from 0.77 to 0.8 (Table II). Forests have smaller clumping index values than grasslands and croplands. The means of the clumping index for forests range from 0.63 to 0.77. During April and September in years from 2003 to 2008, the means of the minimum and maximum clumping index are 0.61 and 0.71 for needle-leaf forests, respectively. These values are 0.62 and 0.83 for broadleaf forests, respectively. During the growing seasons, deciduous forests generally have smaller means and standard deviations of the clumping index than the evergreen forests. However, closed broadleaf deciduous forests are an exception and have the largest mean clumping index and smallest standard deviation among all types of forests.

The comparison of the product with existing/previous satellite products is part of the validation protocol defined by the Committee Earth Observing Satellites Land Product Validation Subgroup [51]. The topographically corrected mean clumping index map based on POLDER-3 data over China's landmass at 6-km resolution produced by Pisek *et al.* [29] is also shown here (Fig. 10). In most areas, the spatial patterns of the clumping index retrieved from the MODIS and POLDER-3 data are similar. The clumping index derived from MODIS at 500-m resolution is generally larger than that derived from POLDER-3 at 6-km resolution in northern China. However, the opposite is true in southern China. The clumping index retrievals from MCD43A1 are 0.05 and 0.08 smaller than those retrieved from POLDER-3 data for open broadleaf deciduous forests and needle-leaf evergreen forests (Table II). For broadleaf evergreen forests, needle-leaf deciduous forests, mosaic of tree cover/other natural vegetation, closed-open evergreen shrubs, the averages of the mean clumping index retrieved from the MCD43A1 product are almost equal to those retrieved from POLDER-3 data. For grasslands and croplands, the clumping index values retrieved from MCD43A1 are slightly larger than those retrieved from POLDER-3 data with the difference between them in the range from 0.03 to 0.05. For other land cover types, the clumping index values retrieved from MCD43A1 are larger than those retrieved from POLDER-3 data, and the differences between them are in the range 0.08 to 0.14. The standard deviations of POLDER-3 retrievals are much larger than those of MODIS retrievals for each land cover type (Table II). However, the relative differences among cover types of the standard deviations of POLDER-3 retrievals

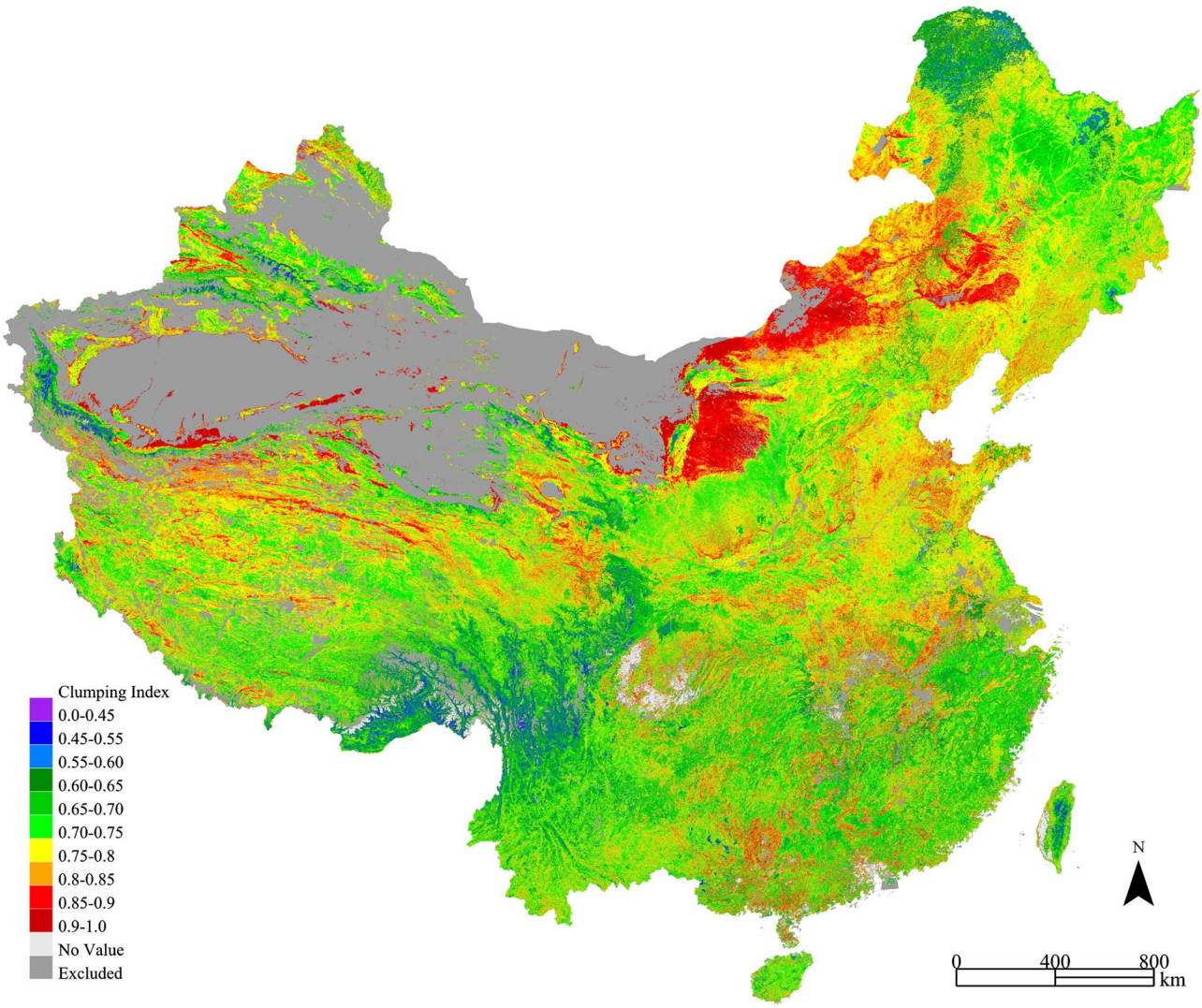

Fig. 8. Spatial distribution of the topographically corrected MODIS-based clumping index averaged over the growing seasons (from April to September) from 2003 to 2008 over China's landmass. The nonvegetation pixels including water bodies, snow and ice, artificial surfaces, and bare areas are excluded in the clumping index map.

are smaller than those of MODIS retrievals. Theoretically, the clumping index derived from POLDER-3 and from MODIS will be same for a homogenous landscape. The relatively coarse spatial resolution of the POLDER-3 pixels probably smoothes the interclass variability of the retrieved clumping index because most POLDER-3 pixels are actually heterogeneous. On the other hand, the across-biome heterogeneity of POLDER-3 pixels might enlarge the within-class variability of the retrieved clumping index due to the large difference in the retrieved clumping index among different land cover types. There are visible errors of the clumping index retrievals from POLDER-3 data in southern China where these values are generally larger than 0.85 for most forest pixels (Fig. 10), which may be due to the lack of high quality POLDER-3 observations in these areas with frequent cloud covers. We believe that the clumping index values retrieved from MCD43A1 are more rational than those retrieved from POLDER-3 data in China.

The retrieved clumping index demonstrates distinguishable seasonal variations. Fig. 11 shows the monthly mean values of clumping index averaged over the 6 years for eight dominant cover types across the country. The needle-leaf deciduous forests have smaller clumping index values in summer than in other seasons. This could be due to the fact that the canopy becomes more clumped in the summer when the crowns become much denser due to needle growth in the spring. Other cover types generally have the maximal clumping index values in April and August. Some of these seasonal variations could result from the fact that the solar zenith angle is fixed in our algorithm for determining the hotspot and darkspot, while the actual solar zenith angle during MODIS image acquisition varies greatly with season. However, the general pattern of smaller clumping index values (more clumped) in the midsummer could be due to the effect the canopy becomes denser (casting more shadows) after the spring growth. The needle-leaf evergreen forests exhibit the smallest annual change in clumping index, ranging from 0.64 to 0.68 because of their stable canopy structure. The shoot-level clumping variation with season due to new needle growth and old needle fall is not well detected by NDHD, although there is a small decrease in the early summer possibly due to the new needle growth making

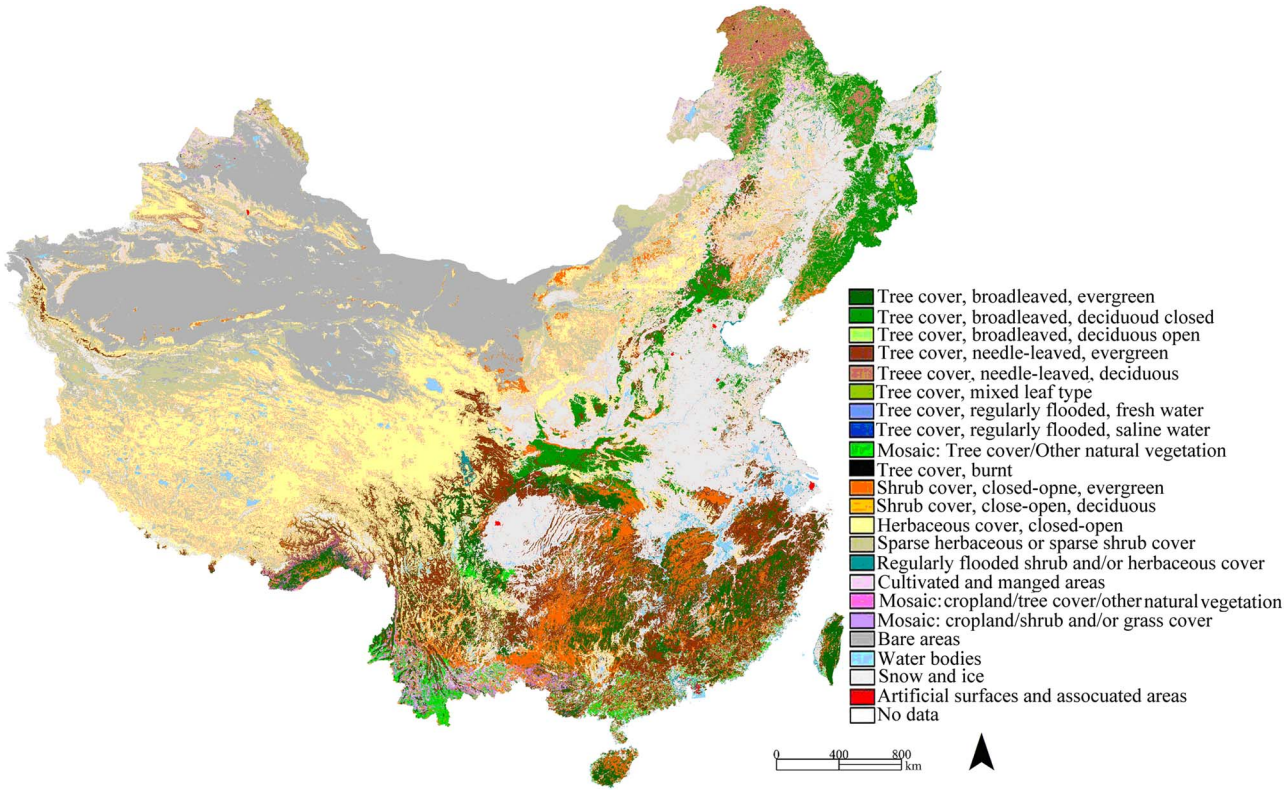

Fig. 9. GLC2000 land cover map of China's landmass at 1-km resolution (Global Land Cover 2000 database. European Commission, Joint Research Centre, 2003).

TABLE II
STATISTICS OF TOPOGRAPHICALLY CORRECTED CLUMPING INDEX DERIVED FROM MODIS BRDF MODEL PARAMETER PRODUCT FOR DIFFERENT LAND COVER TYPES DURING THE GROWING SEASONS (FROM APRIL TO SEPTEMBER) IN YEARS FROM 2003 TO 2008

Cover Type	MODIS Min*	MODIS Max*	MODIS Mean*	STDV of MODIS mean**	POLDER Mean***	STDV of POLDER mean**
Tree Cover, broadleaved, evergreen	0.65	0.81	0.73	0.08	0.73	0.16
Tree Cover, broadleaved, deciduous, closed	0.71	0.83	0.77	0.04	0.65	0.1
Tree Cover, broadleaved, deciduous, open	0.62	0.75	0.67	0.07	0.72	0.15
Tree Cover, needle-leaved, evergreen	0.63	0.71	0.66	0.05	0.74	0.16
Tree Cover, needle-leaved, deciduous	0.61	0.67	0.63	0.04	0.63	0.17
Tree Cover, mixed leaf type	0.7	0.82	0.76	0.04	0.63	0.17
Mosaic: Tree Cover / Other natural vegetation	0.7	0.83	0.76	0.07	0.77	0.13
Tree Cover, burnt	0.69	0.82	0.75	0.05	0.66	0.15
Shrub Cover, closed-open, evergreen	0.7	0.85	0.77	0.07	0.77	0.14
Shrub Cover, closed-open, deciduous	0.7	0.83	0.76	0.05	0.62	0.17
Herbaceous Cover, closed-open	0.71	0.83	0.77	0.07	0.73	0.14
Sparse herbaceous or sparse shrub cover	0.75	0.85	0.8	0.08	0.75	0.14
Regularly flooded shrub and/or herbaceous cover	0.69	0.84	0.76	0.07	0.73	0.16
Cultivated and managed areas	0.71	0.85	0.78	0.05	0.74	0.14
Mosaic: Cropland / Tree Cover / Other	0.6	0.75	0.67	0.1	0.59	0.15
Mosaic: Cropland / Shrub and/or grass cover	0.7	0.84	0.76	0.05	0.72	0.12

Note: *MODIS Min, MODIS Max, and MODIS Mean are averages of the minimum, maximum, and mean topographically corrected clumping index for different land cover types calculated from the monthly maps of clumping index during the growing seasons in years from 2003 to 2008. **STDV of MODIS mean and POLDER mean are the standard deviations of MODIS Mean and POLDER Mean, respectively. ***POLDER Mean is average clumping index values for different land cover types over China calculated with the topographically corrected mean clumping index map retrieved from POLDER-3 data at 6 km resolution by Pisek *et al*. (2010) [29].

the canopy more clumped. Deciduous needle-leaf forests and cultivated and managed areas have large annual variations in the clumping index, ranging from 0.63 to 0.78 and from 0.72 to 0.81, respectively. Closed broadleaf deciduous forests and evergreen broadleaf forests show very similar magnitudes of seasonal variations in the clumping index.

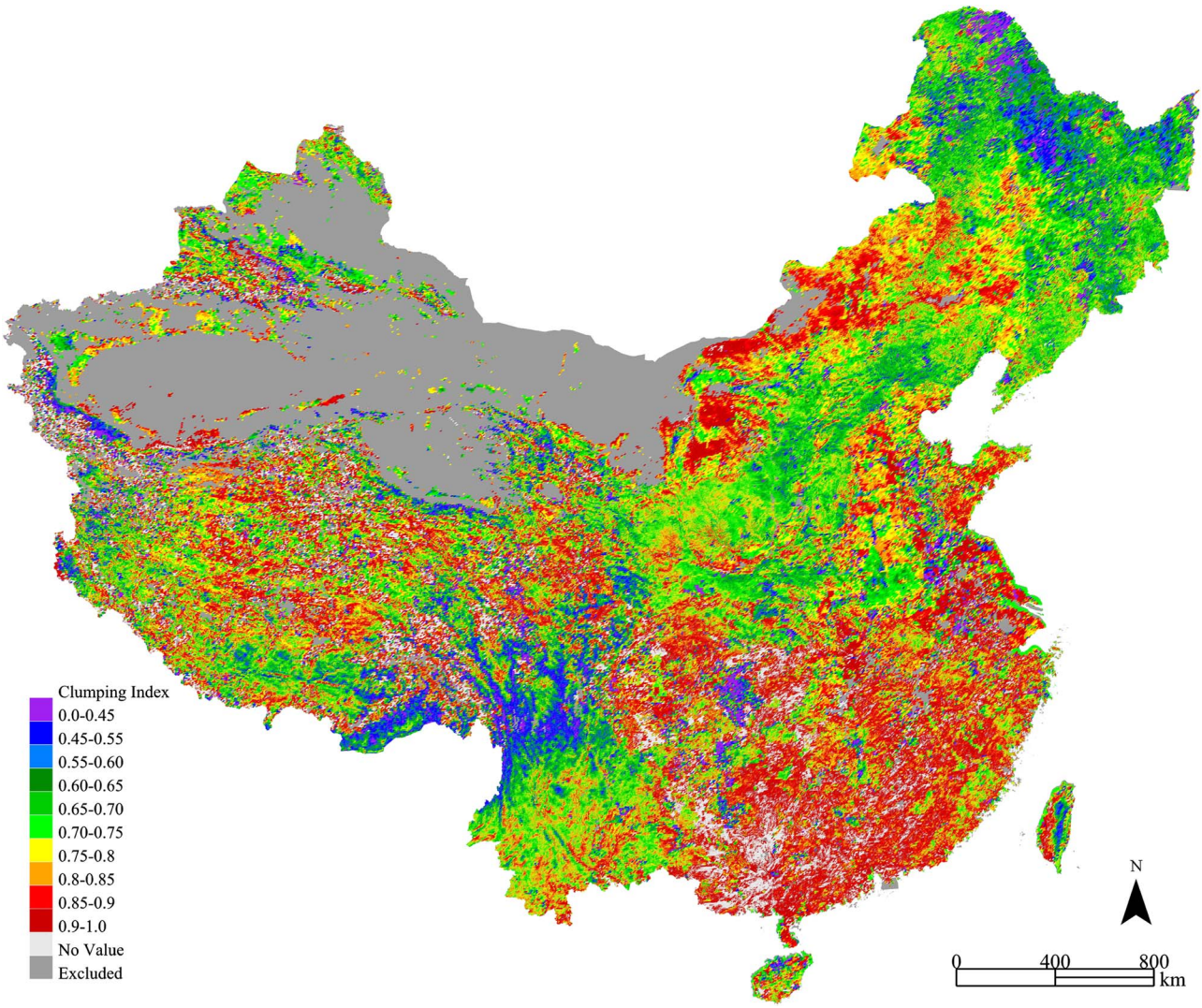

Fig. 10. Topographically corrected mean clumping index map based on POLDER-3 data over China's landmass at 6-km resolution reported by Pisek *et al.* [29].

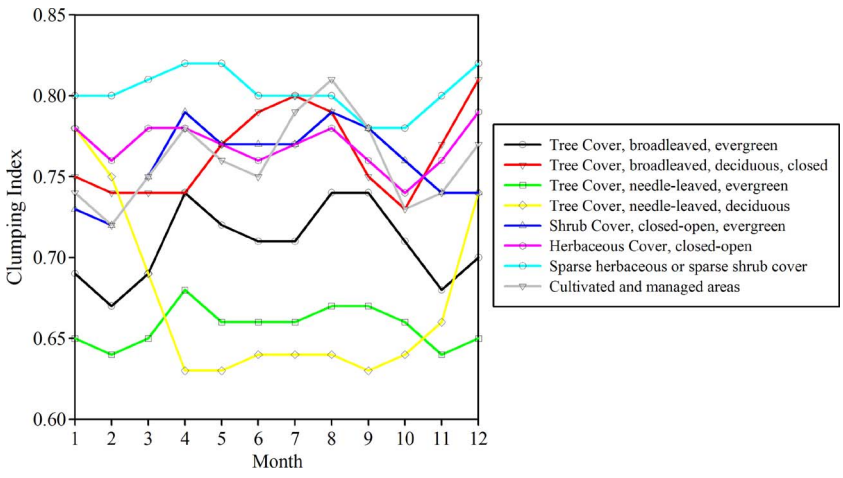

Fig. 11. Mean monthly values of topographically corrected clumping index from 2003 to 2008 for eight dominant cover types in China.

D. Validation of the Retrieved Clumping Index With Field Measurements

Clumping index values retrieved from the MCD43A1 product are compared with current field measurements taken by TRAC at five sites in 2009 (Table III). For several plots, there are no MCD43A1 data with the best or good quality acquired in the same period as field measurements. The clumping index of these plots listed in Table III is derived from the available

TABLE III
COMPARISON OF THE TOPOGRAPHICALLY CORRECTED CLUMPING INDEX DERIVED FROM THE MODIS BRDF MODEL PARAMETER PRODUCTS WITH FIELD MEASUREMENTS TAKEN BY TRAC

Site*	Lat.	Lon.	Vegetation Species	Month of Measurements	γ_E**	Measured Ω_E***	Measured Ω	Month of MODIS Data	Retrieved Ω
QYZ	26.7506	115.0603	Slash Pine, Masson Pine	Apr. 2009	1.45	0.81	0.56	Apr. 2009	0.58
QYZ	26.7489	115.0592	Chinese Fir	Apr. 2009	1.45	0.79	0.54	Apr. 2009	0.60
QYZ	26.7461	115.0661	Chinese Fir	Apr. 2009	1.45	0.74	0.51	Apr. 2009	0.56
QYZ	26.7422	115.0617	Masson Pine	Apr. 2009	1.45	0.77	0.53	Apr. 2009	0.57
QYZ	26.7417	115.0581	Masson Pine	Apr. 2009	1.45	0.76	0.53	Apr. 2009	0.64
QYZ	26.7403	115.0592	Chinese Chestnut	Apr. 2009	1	0.87	0.87	Apr. 2009	0.88
MES	45.3229	127.5434	Larch	Jul. 2009	1.5	0.97	0.65	Jul. 2009	0.58
MES	45.3222	127.5477	Larch	Jul. 2009	1.5	0.93	0.62	Jul. 2009	0.66
MES	45.3219	127.5206	Aspen, Manchurian Ash, Walnut	Jul. 2009	1	0.75	0.75	Jul. 2009	0.76
MES	45.3079	127.5534	Linden, Aspen, Birch	Jul. 2009	1	0.86	0.86	Jul. 2009	0.73
MES	45.3037	127.5163	Mongolian Scotch Pine	Jul. 2009	1.45	0.99	0.68	Jul. 2009	0.58
MES	45.2968	127.5412	Walnut	Jul. 2009	1	0.76	0.76	Jul. 2009	0.68
MES	45.2967	127.5443	Linden, Maple, Elm	Jul. 2009	1	0.89	0.89	Jul. 2009	0.93
MES	45.2966	127.4957	Korean Pine, Camphor Wood	Jul. 2009	1.3	0.97	0.75	Jul. 2009	0.77
MES	45.2957	127.5403	Walnut	Jul. 2009	1	0.81	0.81	Jul. 2009	0.81
MES	45.2954	127.4988	Korean Pine	Jul. 2009	1.5	0.95	0.63	Jul. 2009	0.81
MES	45.2943	127.5145	Mongolian Scotch Pine,Korean Pine	Jul. 2009	1.5	0.97	0.65	Jul. 2009	0.65
MES	45.2813	127.5768	Oak, Aspen, Linden	Jul. 2009	1	0.81	0.81	Jul. 2009	0.85
MES	45.2786	127.577	Mongolian Scotch Pine	Jul. 2009	1.45	0.87	0.6	Jul. 2009	0.65
MES	45.2713	127.5777	Young Aspen	Jul. 2009	1	0.86	0.86	Jul. 2009	0.86
MES	45.2666	127.5767	Larch	Jul. 2009	1.5	0.97	0.65	Jul. 2009	0.68
MES	45.2659	127.578	Larch	Jul. 2009	1.5	0.93	0.62	Jul. 2009	0.63
MES	45.3080	127.5593	Linden,Oak,Elm	Jul. 2009	1.00	0.89	0.89	Jul. 2009	0.79
CBS	42.3234	128.1197	Birch, Aspen	Jul. 2009	1	0.85	0.85	Jul. 2009	0.81
HB	37.6649	106.3314	Shrub, Alpine Meadow	Aug.2009	1	0.69	0.69	Aug.2009	0.80
TTS	29.8553	121.7395	Castanopsis Sclerophylla	Sep. 2009	1	0.91	0.91	Sep. 2009	0.91
TTS	29.8539	121.738	Japan Cedar	Sep. 2009	1.4	0.93	0.66	Sep. 2009	0.68
TTS	29.8538	121.6956	Schima Superba	Sep. 2009	1	0.88	0.88	Sep. 2009	0.92
TTS	29.8538	121.7006	Chinese Fir	Sep. 2009	1.5	0.9	0.6	Sep. 2009	0.77
TTS	29.8526	121.7071	Cyclobalanopsis Glauca	Sep. 2009	1	0.88	0.88	Sep. 2009	0.94
TTS	29.8432	121.748	Castanopsis Sclerophylla	Sep. 2009	1	0.88	0.88	Sep. 2009	0.81
TTS	29.8421	121.7463	Castanopsis Sclerophylla	Sep. 2009	1	0.78	0.78	Sep. 2009	0.84
TTS	29.8043	121.7978	Bamboo	Sep. 2009	1	0.83	0.83	Jul. 2008	0.79
TTS	29.8024	121.7884	Schima Superba	Sep. 2009	1	0.75	0.75	Jul. 2008	0.80
TTS	29.7978	121.7536	Masson Pine	Sep. 2009	1.45	0.83	0.57	Sep. 2009	0.75
TTS	29.7963	121.8038	Bamboo	Sep. 2009	1	0.91	0.91	Jul. 2008	0.87
TTS	29.7961	121.7318	Castanopsis Sclerophylla	Sep. 2009	1	0.8	0.8	Sep. 2009	0.81
TTS	29.7843	121.8061	Japan Cedar	Sep. 2009	1.4	0.94	0.67	Jul. 2008	0.69
TTS	29.7835	121.8019	Japan cedar, Chinese Fir	Sep. 2009	1.5	0.81	0.54	Jul. 2008	0.53
TTS	29.7832	121.8103	Golden Larch, Cypress	Sep. 2009	1.5	0.89	0.59	Jul. 2008	0.52
TTS	29.7755	121.7513	Chinese Fir	Sep. 2009	1.5	0.94	0.63	Jul. 2008	0.67
TTS	29.8103	121.7892	Castanopsis Sclerophylla	Sep. 2009	1.00	0.84	0.84	Jul. 2008	0.65
TTS	29.8065	121.7873	Schima Superba	Sep. 2009	1.00	0.85	0.85	Jul. 2008	0.76
TTS	29.8012	121.7937	Cyclobalanopsis Glauca	Sep. 2009	1.00	0.90	0.90	Jul. 2008	0.77
TTS	29.7846	121.8082	Large sapling	Sep. 2009	1.00	0.84	0.84	Jul. 2008	0.76
TTS	29.7783	121.7619	Bamboo	Sep. 2009	1.00	0.90	0.90	Jul. 2008	0.75

Note: *QYZ, Qianyanzhou; CBS, Changbaishan; MES, Maoershan; HB, Haibei; TTS, Tiantongshan. **γ_E is the ratio of needles to shoots determined by empirical values [49], [50]. ***Ω_E is the element clumping index measured by TRAC.

MCD43A1 data in the same period of 2008. If several plots of field measurements are located within a MODIS pixel, the clumping index values of these plots are averaged to compare with MODIS retrievals.

The agreement between retrieved and measured clumping index is satisfactory, with a R^2 value of 0.61 $(N = 46)$ and a RMSE value of 0.08 (Fig. 12). It is obvious that the intraclass variability of the measured clumping index of needle-leaf forests or broadleaf forests is quite large in these sites. On average, the measured clumping index of needle-leaf forests is smaller than that of broadleaf forests. The average of the retrieved clumping index for these 46 pixels is almost equal to that of field measurements. The largest difference between measured and retrieved results occurs in several Korean Pine, Masson Pine, and bamboo stands (Table III). These disagreements might be attributable to the following factors. First, the size of MODIS pixels is much larger than field measurement plots. In this paper, the retrieved clumping index of 463.3 m $\times$ 463.3 m pixels is directly compared with measurements at 50 m $\times$ 50 m plots due to the absence of high-resolution maps of the clumping index. The spatial scale effects are not taken into account in such a direct comparison. Second, both the Ω_E measured by TRAC and the Ω derived from the MCD43A1 product are shown to be dependent on the solar zenith angle [48], [53]–[55]. The solar zenith angle is currently assumed to be 45° in the retrieval of clumping index from the MCD43A1 product and different from the solar zenith angle when field measurements were taken. Although the effects on the clumping index retrieved from MODIS data or measured by TRAC from one angular observation are slight [30], [56], the difference in the solar zenith angle between MODIS retrieval and field measurements might induce additional disagreement between measured and retrieved clumping index values to some extent. Third, the 500-m land cover map used in this study is downscaled from the GLC2000 land cover map at 1-km spatial resolution. This simple application of 1-km GLC2000 land cover map might result in uncertainties in retrieved clumping index since the relationships between NDHD and clumping

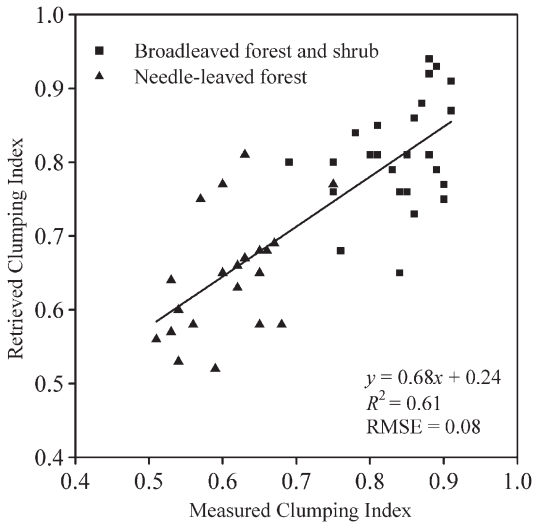

Fig. 12. Comparison of topographically corrected clumping index retrieved from the MODIS BRDF model parameters product with measurements taken by TRAC.

index differ slightly among land cover types, making thematically heterogeneous landscapes appear smooth in the clumping map. Finally, the correlation between clumping index and NDHD is considerably stronger in the NIR band than that in the red band because of the larger amplitude of the reflectance and the lower atmospheric perturbation in the NIR band [17], [42]. However, stronger multiple scattering in the NIR band within vegetation decreases the shadow darkness, making the NIR band less sensitive to changes in vegetation structure than the red band [30].

IV. Conclusion

In this paper, POLDER-3/PARASOL directional reflectance measurements are used as a benchmark to evaluate the ability of the Ross–Li model driven by the MCD43A1 product to simulate MODIS directional reflectance and to optimize the parameters in the modified Ross–Li models. With the reflectance of hotspot and darkspot simulated by one of the best modified models (Ross–Li-H), clumping index maps at 500-m resolution over China's landmass are generated. Using a 90-m resolution DEM, the topographic effects in clumping index maps are removed. According to this study, following conclusions can be drawn.

1) The Ross–Li model effectively reproduces the directional reflectance in most view angles, but it underestimates the NIR hotspot reflectance by 14% compared with POLDER-3 data.
2) Three modifications to the Ross–Li model have all improved the simulation of hotspot reflectance. The algorithm developed in this study to correct the Ross–Li model only needs to determine two parameters [parameters A and B in (10)] for all land cover types and is able to simulate hotpot reflectance based on the MCD43A1 product with satisfactory accuracy, indicating the applicability of this algorithm for correcting the BRDF effect and for retrieving the clumping index.
3) Retrieved clumping index values correlate well with field measurements ($R^2 = 0.61$), indicating the feasibility of the algorithm developed in this study for retrieving the clumping index from the MCD43A1 product. The retrieved mean clumping index map over China's landmass shows distinct spatial patterns closely related to land cover types. Different cover types also show different seasonal variation patterns when averaged for the period from 2003 to 2008.
4) Compared with the previous POLDER-based clumping index at 6-km resolution, the 500-m resolution MODIS-based clumping index can provide more reasonably accurate and up-to-date vegetation structure information for modeling of terrestrial energy, carbon, and water cycle processes, particularly in the heterogeneous vegetated areas.

Acknowledgment

The MODIS BRDF data are distributed by the LP DAAC. The POLDER-3/PARASOL BRDFs databases have been elaborated by the LSCE and provided by the POSTEL Service Centre. The POLDER-3/PARASOL data are from CNES. The authors would like to thank two anonymous reviewers for helping to improve this paper.

References

[1] T. Nilson, "Theoretical analysis of frequency of gaps in plant stands," *Agric. Meteorol.*, vol. 8, no. 1, pp. 25–38, 1971.
[2] J. M. Chen, "Optically-based methods for measuring seasonal variation of leaf area index in boreal conifer stands," *Agric. Forest Meteorol.*, vol. 80, no. 2–4, pp. 135–163, Jul. 1996.
[3] D. D. Baldocchi and K. B. Wilson, "Modeling CO_2 and water vapor exchange of a temperate broadleaved forest across hourly to decadal time scales," *Ecol. Model.*, vol. 142, no. 1–2, pp. 155–184, Aug. 2001.
[4] J. M. Chen, J. Liu, S. G. Leblanc, R. Lacaze, and J. L. Roujean, "Multi-angular optical remote sensing for assessing vegetation structure and carbon absorption," *Remote Sens. Environ.*, vol. 84, no. 4, pp. 516–525, Apr. 2003.
[5] J. M. Chen and T. A. Black, "Measuring leaf-area index of plant canopies with branch architecture," *Agric. Forest Meteorol.*, vol. 57, no. 1–3, pp. 1–12, Dec. 1991.
[6] C. J. Kucharik, J. M. Norman, L. M. Murdock, and S. T. Gower, "Characterizing canopy nonrandomness with a multiband vegetation imager (MVI)," *J. Geophys. Res.*, vol. 102, no. D24, pp. 29 455–29 473, 1997.
[7] J. L. Roujean and R. Lacaze, "Global mapping of vegetation parameters from POLDER multiangular measurements for studies of surface-atmosphere interactions: A pragmatic method and its validation," *J. Geophys. Res.*, vol. 107, no. D12, pp. 10 129–10 145, Jun. 2002.
[8] M. Weiss, F. Baret, S. Garrigues, and R. Lacaze, "LAI and fAPAR CYCLOPES global products derived from VEGETATION. Part 2: Validation and comparison with MODIS collection 4 products," *Remote Sens. Environ.*, vol. 110, no. 3, pp. 317–331, Oct. 2007.
[9] D. D. Baldocchi, K. B. Wilson, and L. H. Gu, "How the environment, canopy structure and canopy physiological functioning influence carbon, water and energy fluxes of a temperate broad-leaved deciduous forest-an assessment with the biophysical model CANOAK," *Tree Physiol.*, vol. 22, no. 15/16, pp. 1065–1077, Nov. 2002.
[10] Q. Chen, D. Baldocchi, P. Gong, and T. Dawson, "Modeling radiation and photosynthesis of a heterogeneous savanna woodland landscape with a hierarchy of model complexities," *Agric. Forest Meteorol.*, vol. 148, no. 6/7, pp. 1005–1020, Jun. 2008.
[11] J. Liu, J. M. Chen, and J. Cihlar, "Mapping evapotranspiration based on remote sensing: An application to Canada's landmass," *Water Resour. Res.*, vol. 39, no. 7, pp. 1189–1200, Jul. 2003.
[12] T. Nilson, "Inversion of gap frequency data in forest stands," *Agric. Forest Meteorol.*, vol. 98/99, no. 31, pp. 437–448, Dec. 1999.

[13] Y. Ryu, O. Sonnentag, T. Nilson, R. Vargas, H. Kobayashi, R. Wenk, and D. D. Baldocchi, "How to quantify tree leaf area index in an open savanna ecosystem: A multi-instrument and multi-model approach," *Agric. Forest Meteorol.*, vol. 150, no. 1, pp. 63–76, Jan. 2010.

[14] J. M. Chen and J. Cihlar, "Plant canopy gap-size analysis theory for improving optical measurements of leaf-area index," *Appl. Opt.*, vol. 34, no. 27, pp. 6211–6222, Sep. 1995.

[15] V. Demarez, S. Duthoit, F. Baret, M. Weiss, and G. Dedieu, "Estimation of leaf area and clumping indexes of crops with hemispherical photographs," *Agric. Forest Meteorol.*, vol. 148, no. 4, pp. 644–655, Apr. 2008.

[16] A. Gonsamo and P. Pellikka, "The computation of foliage clumping index using hemispherical photography," *Agric. Forest Meteorol.*, vol. 149, no. 10, pp. 1781–1787, Oct. 2009.

[17] A. Simic, J. M. Chen, J. R. Freemantle, J. R. Miller, and J. Pisek, "Improving clumping and LAI algorithms based on multiangle airborne imagery and ground measurements," *IEEE Trans. Geosci. Remote Sens.*, vol. 48, no. 4, pp. 1742–1759, Apr. 2010.

[18] Y. Ryu, T. Nilson, H. Kobayashi, O. Sonnentag, B. E. Law, and D. D. Baldocchi, "On the correct estimation of effective leaf area index: Does it reveal information on clumping effects?"*Agric. Forest Meteorol.*, vol. 150, no. 3, pp. 463–472, Mar. 2010.

[19] R. Liu, J. M. Chen, J. Liu, F. Deng, and R. Sun, "Application of a new leaf area index algorithm to China's landmass using MODIS data for carbon cycle research," *J. Environ. Manage.*, vol. 85, no. 3, pp. 649–658, Nov. 2007.

[20] Y. J. Wang, C. E. Woodcock, W. Buermann, P. Stenberg, P. Voipio, H. Smolander, T. Hame, Y. H. Tian, J. N. Hu, Y. Knyazikhin, and R. B. Myneni, "Evaluation of the MODIS LAI algorithm at a coniferous forest site in Finland," *Remote Sens. Environ.*, vol. 91, no. 1, pp. 114–127, May 2004.

[21] R. Lacaze, J. M. Chen, J. L. Roujean, and S. G. Leblanc, "Retrieval of vegetation clumping index using hot spot signatures measured by POLDER instrument," *Remote Sens. Environ.*, vol. 79, no. 1, pp. 84–95, Jan. 2002.

[22] F. Gao, C. B. Schaaf, A. H. Strahler, Y. Jin, and X. Li, "Detecting vegetation structure using a kernel-based BRDF model," *Remote Sens. Environ.*, vol. 86, no. 2, pp. 198–205, Jul. 2003.

[23] B. Pinty, J. L. Widlowski, N. Gobron, M. M. Verstraete, and D. J. Diner, "Uniqueness of multiangular measurements—Part I: An indicator of subpixel surface heterogeneity from MISR," *IEEE Trans. Geosci. Remote Sens.*, vol. 40, no. 7, pp. 1560–1573, Jul. 2002.

[24] S. Sandmeier, C. Muller, B. Hosgood, and G. Andreoli, "Physical mechanisms in hyperspectral BRDF data of grass and watercress," *Remote Sens. Environ.*, vol. 66, no. 2, pp. 222–233, Nov. 1998.

[25] S. Sandmeier and D. W. Deering, "Structure analysis and classification of boreal forests using airborne hyperspectral BRDF data from ASAS," *Remote Sens. Environ.*, vol. 69, no. 3, pp. 281–295, Sep. 1999.

[26] J. Pisek, J. M. Chen, J. R. Miller, J. R. Freemantle, J. I. Peltoniemi, and A. Simic, "Mapping forest background reflectance in a boreal region using multiangle compact airborne spectrographic imager data," *IEEE Trans. Geosci. Remote Sens.*, vol. 48, no. 1, pp. 499–510, Jan. 2010.

[27] G. Yang, C. Zhao, Q. Liu, W. Huang, and J. Wang, "Inversion of a radiative transfer model for estimating forest LAI from multisource and multiangular optical remote sensing data," *IEEE Trans. Geosci. Remote Sens.*, vol. 49, no. 3, pp. 988–1000, Mar. 2011.

[28] J. M. Chen, J. Liu, S. G. Leblanc, J. L. Roujean, and R. Lacaze, "Utility of multi-angle remote sensing for terrestrial carbon cycle modeling," in *Proc. 8th Int. Symp. Phys. Signatures Meas. Remote Sens.*, Aussois, France, Jan. 2001.

[29] J. Pisek, J. M. Chen, R. Lacaze, O. Sonnentag, and K. Alikas, "Expanding global mapping of the foliage clumping index with multi-angular POLDER three measurements: Evaluation and topographic compensation," *ISPRS J. Photogramm. Remote Sens.*, vol. 65, no. 4, pp. 341–346, Jul. 2010.

[30] J. M. Chen, C. H. Menges, and S. G. Leblanc, "Global mapping of foliage clumping index using multi-angular satellite data," *Remote Sens. Environ.*, vol. 97, no. 4, pp. 447–457, Sep. 2005.

[31] S. G. Leblanc, J. M. Chen, H. P. White, and R. Latifovic, "Canadawide foliage clumping index mapping from multi-angular POLDER measurements," *Can. J. Remote Sens.*, vol. 31, no. 5, pp. 364–376, Oct. 2005.

[32] J. L. Privette, Y. Tian, G. Roberts, R. J. Scholes, Y. Wang, K. K. Caylor, P. Frost, and M. Mukelabai, "Vegetation structure characteristics and relationships of Kalahari woodlands and savannas," *Global Change Biol.*, vol. 10, no. 3, pp. 281–291, Mar. 2004.

[33] O. Hautecoeur and M. M. Leroy, "Surface bidirectional reflectance distribution function observed at global scale by POLDER/ADEOS," *Geophys. Res. Lett.*, vol. 25, no. 22, pp. 4197–4200, Nov. 1998.

[34] P. Y. Deschamps, F. M. Breon, M. Leroy, A. Podaire, A. Bricaud, J. C. Buriez, and G. Seze, "The POLDER mission: Instrument characteristics and scientific objectives," *IEEE Trans. Geosci. Remote Sens.*, vol. 32, no. 3, pp. 598–615, May 1994.

[35] W. Lucht, C. B. Schaaf, and A. H. Strahler, "An algorithm for the retrieval of albedo from space using semiempirical BRDF models," *IEEE Trans. Geosci. Remote Sens.*, vol. 38, no. 2, pp. 977–998, Mar. 2000.

[36] J. L. Roujean, M. Leroy, and P. Y. Deschamps, "A bidirectional reflectance model of the Earth's surface for the correction of remote-sensing data," *J. Geophys. Res.*, vol. 97, no. D18, pp. 20 455–20 468, Dec. 1992.

[37] C. B. Schaaf, F. Gao, A. H. Strahler, W. Lucht, X. W. Li, T. Tsang, N. C. Strugnell, X. Y. Zhang, Y. F. Jin, J. P. Muller, P. Lewis, M. Barnsley, P. Hobson, M. Disney, G. Roberts, M. Dunderdale, C. Doll, R. P. d'Entremont, B. X. Hu, S. L. Liang, J. L. Privette, and D. Roy, "First operational BRDF, albedo nadir reflectance products from MODIS," *Remote Sens. Environ.*, vol. 83, no. 1/2, pp. 135–148, Nov. 2002.

[38] W. Wanner, A. H. Strahler, B. Hu, P. Lewis, J. P. Muller, X. Li, C. L. B. Schaaf, and M. J. Barnsley, "Global retrieval of bidirectional reflectance and albedo over land from EOS MODIS and MISR data: Theory and algorithm," *J. Geophys. Res.*, vol. 102, no. D14, pp. 17 143–17 161, 1997.

[39] O. Hautecoeur and M. Leroy, "An accuracy assessment experiment of the BRDF measured at coarse spatial resolution from space," *Int. J. Remote Sens.*, vol. 21, no. 15, pp. 2957–2963, 2000.

[40] J. M. Chen and S. G. Leblanc, "A four-scale bidirectional reflectance model based on canopy architecture," *IEEE Trans. Geosci. Remote Sens.*, vol. 35, no. 5, pp. 1316–1337, Sep. 1997.

[41] J. M. Chen and J. Cihlar, "A hotspot function in a simple bidirectional reflectance model for satellite applications," *J. Geophys. Res.*, vol. 102, no. D22, pp. 25 907–25 913, Nov. 1997.

[42] F. Maignan, F. M. Bréon, and R. Lacaze, "Bidirectional reflectance of Earth targets: Evaluation of analytical models using a large set of spaceborne measurements with emphasis on the hot spot," *Remote Sens. Environ.*, vol. 90, no. 2, pp. 210–220, Mar. 2004.

[43] F. M. Bréon, F. Maignan, M. Leroy, and I. Grant, "Analysis of hot spot directional signatures measured from space," *J. Geophys. Res.*, vol. 107, no. D16, p. 4282, Aug. 2002.

[44] K. Hasegawa, H. Matsuyama, H. Tsuzuki, and T. Sweda, "Improving the estimation of leaf area index by using remotely sensed NDVI with BRDF signatures," *Remote Sen. Environ.*, vol. 114, no. 3, pp. 514–519, Mar. 2010.

[45] N. Rochdi, R. Fernandes, and M. Chelle, "An assessment of needles clumping within shoots when modeling radiative transfer within homogeneous canopies," *Remote Sens. Environ.*, vol. 102, no. 1/2, pp. 116–134, May 2006.

[46] M. J. Hill, C. Averill, Z. Jiao, C. B. Schaaf, and J. D. Armston, "Relationship of MISR RPV parameters and MODIS BRDF shape indicators to surface vegetation patterns in an Australian tropical savanna," *Can. J. Remote Sens.*, vol. 34, no. S2, pp. S247–S267, 2008.

[47] C. B. Schaaf, X. W. Li, and A. H. Strahler, "Topographic effects on bidirectional and hemispherical reflectances calculated with a geometric-optical canopy model," *IEEE Trans. Geosci. Remote Sens.*, vol. 32, no. 6, pp. 1186–1193, Nov. 1994.

[48] J. M. Chen, P. M. Rich, S. T. Gower, J. M. Norman, and S. Plummer, "Leaf area index of boreal forests: Theory, techniques, and measurements," *J. Geophys. Res.*, vol. 102, no. D24, pp. 29 429–29 443, Dec. 1997.

[49] J. M. Chen, A. Govind, O. Sonnentag, Y. Q. Zhang, A. Barr, and B. Amiro, "Leaf area index measurements at Fluxnet-Canada forest sites," *Agric. Forest Meteorol.*, vol. 140, no. 1–4, pp. 257–268, Nov. 2006.

[50] S. T. Gower, C. J. Kucharik, and J. M. Norman, "Direct and indirect estimation of leaf area index, fAPAR and net primary production of terrestrial ecosystems," *Remote Sens. Environ.*, vol. 70, no. 1, pp. 29–51, Oct. 1999.

[51] J. T. Morisette, F. Baret, J. L. Privette, R. B. Myneni, J. E. Nickeson, S. Garrigues, N. V. Shabanov, M. Weiss, R. A. Fernandes, S. G. Leblanc, M. Kalacska, G. A. Sanchez-Azofeifa, M. Chubey, B. Rivard, P. Stenberg, M. Rautiainen, P. Voipio, T. Manninen, A. N. Pilant, T. E. Lewis, J. S. Iiames, R. Colombo, M. Meroni, L. Busetto, W. B. Cohen, D. P. Turner, E. D. Warner, G. W. Petersen, G. Seufert, and R. Cook, "Validation of global moderate-resolution LAI products: A framework proposed within the CEOS land product validation subgroup," *IEEE Trans. Geosci. Remote Sens.*, vol. 44, no. 7, pp. 1804–1817, Jul. 2006.

[52] W. Wanner, X. Li, and A. H. Strahler, "On the derivation of kernels for kernel-driven of bidirectional reflectance," *J. Geophys. Res.*, vol. 100, no. D10, pp. 21 077–21 090, Oct. 1995.

[53] S. Duthoit, V. Demarez, J. P. Gastellu-Etchegorry, E. Martin, and J. L. Roujean, "Assessing the effects of the clumping phenomenon on

BRDF of a maize crop based on 3D numerical scenes using DART model," *Agric. Forest Meteorol.*, vol. 148, no. 8/9, pp. 1341–1352, Jul. 2008.

[54] C. J. Kucharik, J. M. Norman, and S. T. Gower, "Characterization of radiation regimes in nonrandom forest canopies: Theory, measurements, and a simplified modeling approach," *Tree Physiol.*, vol. 19, no. 11, pp. 695–706, Sep. 1999.

[55] F. Montes, P. Pita, A. Rubio, and I. Canellas, "Leaf area index estimation in mountain even-aged Pinus silvestris L. stands from hemispherical photographs," *Agric. Forest Meteorol.*, vol. 145, no. 3/4, pp. 215–228, Aug. 2007.

[56] W. Ni-Meister, W. Z. Yang, and N. Y. Kiang, "A clumped-foliage canopy radiative transfer model for a global dynamic terrestrial ecosystem model I: Theory," *Agric. Forest Meteorol.*, vol. 150, no. 7/8, pp. 895–905, Jul. 2010.

Gaolong Zhu received the B.S. degree in geography from Beijing Normal University, Beijing, China, in 1997, the M.S. degrees in cartography and geographic information system (GIS) from Peking University, Beijing, China, in 2003, and the Ph.D. degree in cartography and GIS from Nanjing University, Nanjing, China, in 2011.

He is currently an Associate Professor with the Department of Geography, Minjiang University, Fuzhou, China. His current research interests include modeling and inversion of multi-angular remote sensing data.

Weimin Ju received the B.Sc. degree from the Nanjing Institute of Meteorology in China, in 1984, and the M.Sc. and Ph.D. degrees from University of Toronto, Toronto, ON, Canada, in 2002 and 2006, respectively.

He is currently a Professor at the International Institute for Earth System Sciences, Nanjing University, Nanjing, China. His major research interest includes retrieval of vegetation parameters from remote sensing data and simulating terrestrial carbon and water fluxes. He has published over 80 papers in refereed journals, including 31 papers in international journals.

Jing M. Chen received the B.Sc. degree from the Nanjing Institute of Meteorology in China, in 1982, and the Ph.D. degree from Reading University, Reading, U.K., in 1986.

He is currently a Professor in the Department of Geography and Program in Planning, University of Toronto, Toronto, ON, Canada, Research Chair, and Fellow of the Royal Society of Canada. He is also an Adjunct Professor at Nanjing University, Nanjing, China. His major research interest is in remote sensing of vegetation and quantifying terrestrial carbon and water fluxes. He has published over 200 papers in refereed journals, which have been cited over 5000 times in the scientific literature. He is currently an Associate Editor of the *Journal of Geophysical Research—Atmosphere*, *Canadian Journal of Remote Sensing*, and *Journal of Applied Remote Sensing*.

Peng Gong received the B.S. and M.S. degrees in geography from Nanjing University, Nanjing, China, in 1984 and 1986, respectively, and the Ph.D. degree in geography from the University of Waterloo, Waterloo, ON, Canada, in 1990.

He was a Research Scientist with the Institute for Space and Terrestrial Science, North York, ON, Canada, and an Assistant Professor with the Department of Geomatics Engineering, University of Calgary, Calgary, AB, Canada, before joining the Department of Environmental Science, Policy, and Management, University of California, Berkeley, in 1994, where he became a Full Professor in 2001. He was the Founding Director of the International Institute for Earth System Science, Nanjing University, between 2000 and 2007, and the Founding Director of the State Key Laboratory of Remote Sensing Science, jointly sponsored by the Institute of Remote Sensing Applications, Chinese Academy of Sciences, and Beijing Normal University, Beijing, China, between 2004 and 2010. He became the Director of the Center for Earth System Science, Tsinghua University, Beijing, in 2010. His present interest is environmental remote sensing and global environmental change and health. He has authored/coauthored over 400 publications including more than 260 journal articles in the field of remote sensing, geography, and environmental science and six books.

Bailing Xing received the B.S. degree in geographic information system from XinYang Normal University, Henan, China, in 2009. She is currently working toward the M.S. degree at Nanjing University, Jiangsu, China.

Her research interests include leaf area index retrieval and assessing the impact of urbanization on regional net primary productivity.

Jingfang Zhu received the B.S. degrees in geographic information system (GIS) from Zhengzhou University, Zhengzhou, China, in 2009, and is currently working toward the M.S. degree in cartography and GIS at the Nanjing University, Nanjing, China.

Her research interests cover the retrieval of biophysical parameters (e.g., leaf area index and clumping index) from remotely sensed data.